



Glass-forming ability and corrosion performance of Mn-doped Mg–Zn–Ca amorphous alloys for biomedical applications

Jian-Li Wang* , Yin Wan, Zhi-Jun Ma, Yong-Chun Guo, Zhong Yang, Ping Wang, Jian-Ping Li

Received: 19 April 2017/Revised: 14 August 2017/Accepted: 19 March 2018/Published online: 13 April 2018
© The Nonferrous Metals Society of China and Springer-Verlag GmbH Germany, part of Springer Nature 2018

Abstract In the present work, ribbon and 2-mm rod samples of Mg–Zn–Ca–Mn alloys were prepared by melt-spinning and copper mold injection methods, respectively. Effects of Mn doping on glass-forming ability and corrosion performance in simulated body fluid of Mg₆₅Zn₃₀Ca₅ alloy were studied through X-ray diffraction, scanning electron microscopy, differential scanning calorimeter, and electrochemical and immersion tests. Results show that with the Mn addition increasing, all the ribbon samples are completely in amorphous state. However, the microstructure of 2-mm rod samples transfers from fully amorphous for the Mn-free alloy to almost polycrystalline state with precipitated Mg, Mn, and MgZn phases. Glass-forming ability of Mg₆₅Zn₃₀Ca₅ alloy is decreased by Mn addition. Results of electrochemical and immersion tests demonstrate that the Mn-doped samples exhibit more negative corrosion potential and larger corrosion current density, suggesting that the corrosion resistance decreases with doping amount of Mn element increasing.

Keywords Mg–Zn–Ca amorphous alloys; Mn doping; Glass-forming ability; Corrosion performance

1 Introduction

Magnesium (Mg) alloys exhibit promising application potential as biomedical metallic materials because of their closer density (1.74–2.0 g·cm⁻³) and elastic modulus

(41–45 GPa) to those of human bone (1.8–2.0 g·cm⁻³, 5–23 GPa) [1] compared with the commonly used stainless steel, titanium-based alloys, and cobalt-chrome alloys. The closer Young's modulus could effectively alleviate the undesirable "shielding stress effect" [2]. In addition, Mg is a macro-element in human body (420 mg·day⁻¹) [3], and it participates in a number of metabolism reactions. The release of Mg ion will stimulate the regeneration of new bone cell and accelerate the growth of bone tissues [4]. Reported studies have also indicated the good biocompatibility [3] and bio-resorbability [5, 6] of devices such as cardiovascular stent fabricated by Mg alloys [7].

However, Mg-based implants will face the aggressive physiological environment (high concentration of Cl⁻) when they are implanted in human body, which would lead to the rapid degradation of implants matrix and undesirable hydrogen evolution by the corrosion reaction $Mg + 2H_2O \rightarrow Mg^{2+} + 2OH^- + H_2$. In animal trials, the gradually formed subcutaneous gas bubbles need extra perforation operation to be eliminated [8]. Meanwhile, rapid degradation brings about the rapid dropping of mechanical integrity before the absolute healing of bone tissues, which would result in the most implantation failure. Therefore, up to date, the undesirable corrosion resistance of magnesium alloys is the primary issue that constraints the wide applications such as load-bearing implants. Researchers have done lots of work to seek new strategies to enhance the corrosion resistance. Surface modification is an effective way that could decline the high corrosion rate and protect matrix from quicker degradation [9–11]. Another way is developing new alloy system that possesses better corrosion resistance [12]. However, the corrosion mechanism in principal is just modified but not completely changed. Consequently, only limited improvement in corrosion resistance has been gained.

J.-L. Wang*, Y. Wan, Z.-J. Ma, Y.-C. Guo, Z. Yang, P. Wang, J.-P. Li
School of Materials and Chemical Engineering, Xi'an Technological University, Xi'an 710021, China
e-mail: wjl810325@163.com

Magnesium-based bulk metallic glasses (BMGs) show much stronger corrosion resistance than its crystalline counterpart due to the chemical homogeneity and the absence of second phases as well as other microscopic defects, such as dislocations, grain boundaries, and precipitates [13, 14]. Same as the Mg-based BMGs, their composites also exhibit better corrosion resistance than the as-cast crystallines. In recent years, Mg–Zn–Ca metallic glasses and their composites are considered as ideal candidates for biomedical applications. It is because that human body has a high tolerance limit of Zn ($10 \text{ mg}\cdot\text{day}^{-1}$) and Ca ($1000 \text{ mg}\cdot\text{day}^{-1}$) in daily life [15]. Zberg et al. [16] also reported that $\text{Mg}_{60+x}\text{Zn}_{35-x}\text{Ca}_5$ ($0 \leq x \leq 7$, at%) metallic glasses showed good tissue compatibility and demonstrated a significant improvement in corrosion resistance. In vitro cyto-compatibility and in vivo animal investigations further suggested that Mg–Zn–Ca metallic glasses could satisfy the requisite biocompatibility and constrict the unwanted hydrogen evolution. Recent studies reported by Ravi et al. demonstrated that partially amorphous Mg-based alloys would be promising in the field of biomedical applications [17]. At present, considering that the suitable biodegradable implant should function properly for at least 3 months in vivo [18], more research about bio-safety and biodegradation is still necessary in the future.

Manganese (Mn) is one of the important trace elements in human body, and it is involved in the synthesis and activation of enzymes for human body health [15]. At present, studies about Mn-containing Mg alloys, such as Mg–2.0Zn–0.2Mn [19] and Mg–1.2Mn–1.0Zn [20], have been proposed for biomedical application for their improved corrosion resistance. In the present work, Mg–Zn–Ca alloys with different amounts of Mn addition were prepared through the rapid solidification method by using industrial pure raw materials. The effect of Mn on the glass-forming ability (GFA) and corrosion performance was investigated.

2 Experimental

Alloy ingots with compositions of $(\text{Mg}_{65}\text{Zn}_{30}\text{Ca}_5)_{100-x}\text{Mn}_x$ ($x = 0, 0.2, 0.5, 0.8, 1.2, 1.5$; at%) were prepared by melting industrial pure Mg (99.8 wt%), Zn (99.5 wt%), Mg–30 wt%Ca master alloy, and Mg–10 wt%Mn master alloy in induction furnace under the protection of high-purity argon gas. Then, ribbons of these alloys were fabricated using melt-spinning method. Meanwhile, rods with diameter of 2 mm were prepared by induction re-melting the master alloys in the quartz tube and injecting into water-cooled copper mold. The amorphicity and microstructure of the ribbon and 2-mm (Φ 2mm) rod

samples were characterized by X-ray diffractometer (XRD, Shimadzu XRD-6000) with Cu $K\alpha$ radiation ($\lambda = 0.15418 \text{ nm}$) and scanning electron microscope (SEM, TESCAN VEGA II LMU) equipped with energy-dispersive spectrometry (EDS, Oxford, INCA energy 300). Differential scanning calorimetry (DSC) was employed to investigate the thermal stability using a DSC823e differential scanning calorimeter under the flow of purified argon gas at a heating rate of $20 \text{ K}\cdot\text{min}^{-1}$. The electrochemical tests were carried out at $(310 \pm 1) \text{ K}$ in a beaker containing 1000 ml simulated body fluid (SBF, with a chemical composition same to that in Ref. [21]) on a PARTAT 4000 electrochemical workstation using a standard three-electrode configuration. The studied alloys were served as working electrode. Saturated calomel electrode and platinum electrode were used as reference electrode and counterelectrode, respectively. Open-circuit potentials (OCP) were first monitored for 5400 s. Then potentiodynamic polarization tests were carried out within $\pm 250 \text{ mV}$ range with respect to OCP at a scanning rate of $1 \text{ mV}\cdot\text{s}^{-1}$. For the static immersion tests, 2-mm rod samples were firstly polished until no scratches were present and ultrasonically cleaned by deionized water and ethanol, and then immersed into a beaker containing 150 ml SBF solution. After 12 h, samples were fetched out, rinsed with deionized water and further immersed into chromic acid to remove the corrosion product, then gently washed with deionized water, and dried by cold air. Hydrogen evolution tests were carried out through measuring the released volume of H_2 during the immersion process, and detailed procedures for this testing are similar to that used in Ref. [22]. Samples were immersed in SBF solution up to 24 h, and the released H_2 was collected into a burette, and the volume of evolved hydrogen gas was recorded at regular time intervals.

3 Results and discussion

3.1 Glass-forming ability

Figure 1a shows XRD patterns of the ribbon samples with different amounts of Mn addition. It can be observed that there is only a broad halo peak present at about 38° (2θ) without any other detectable crystalline peaks for all the alloys. It is indicated that the ribbon samples exhibit a completely amorphous structure. Figure 1b displays XRD patterns of the injected 2-mm rods of $(\text{Mg}_{65}\text{Zn}_{30}\text{Ca}_5)_{100-x}\text{Mn}_x$ ($x = 0, 0.2, 0.5, 0.8, 1.2, 1.5$; at%) alloys. As can be seen, the $\text{Mg}_{65}\text{Zn}_{30}\text{Ca}_5$ rod sample has the typical amorphous features without any detectable crystalline peaks. With a minor Mn addition ($x = 0.2$ at%), a weak crystallization peak corresponding to

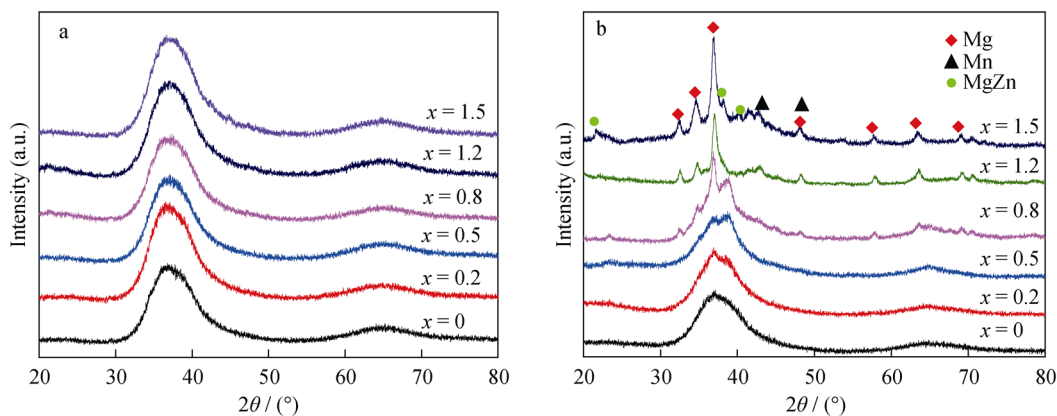


Fig. 1 XRD patterns of $(\text{Mg}_{65}\text{Zn}_{30}\text{Ca}_5)_{100-x}\text{Mn}_x$ alloys: **a** ribbons and **b** 2-mm rods

Mg phase appears. Further increasing addition of Mn results in sharp crystalline peaks (Mg, Mn, and MgZn phases) superimposed on the broad diffraction curves for $(\text{Mg}_{65}\text{Zn}_{30}\text{Ca}_5)_{100-x}\text{Mn}_x$ ($x = 0.5, 0.8, 1.2, 1.5$; at%) rod samples. It can be seen that $(\text{Mg}_{65}\text{Zn}_{30}\text{Ca}_5)_{98.8}\text{Mn}_{1.2}$ and $(\text{Mg}_{65}\text{Zn}_{30}\text{Ca}_5)_{98.5}\text{Mn}_{1.5}$ alloys tend to be of almost fully crystalline structure.

Figure 2 presents SEM backscattered electron (BSE) images of Mg–Zn–Ca–Mn rod samples. Figure 2a shows no distinct segregation and other micro-defects in the backscattered electron image, which demonstrates the completely amorphous structure of $\text{Mg}_{65}\text{Zn}_{30}\text{Ca}_5$ rod sample. With a small amount addition of Mn ($x = 0.2$ at%), a few extremely fine dendrite phases precipitate on the amorphous matrix, as shown in Fig. 2b. The content and size of dendrite phases increase with the further addition of Mn, as shown in Fig. 2c–f. Meanwhile, bright white

particles dispersing around the black dendrite phases or gathering on the remaining gray phases are observed in Fig. 2d–f. The newly formed phases precipitated in the amorphous matrix for the 2-mm rod samples were analyzed by EDS, and the results are listed in Table 1. It is shown in Fig. 2e that Mg content in the black dendrite phase (labeled as A) is about 77.91 at%. Thus, it can be confirmed as Mg phase according to XRD results. For the light-gray phases (labeled as B in Fig. 2e) distributing along the Mg phase, EDS result indicates that the Mg and Zn contents are 56.94 at% and 39.31 at%, respectively. Based on XRD results, it can be identified as (Mg + MgZn) eutectics [23, 24]. While for the bright white particle (labeled as C) in Fig. 2f, EDS analysis reveals that it consists of a large amount of Mn element. Combining with XRD results, it can be confirmed as Mn phase. The higher Mg content is resulted from the energy spectrum drift from matrix.

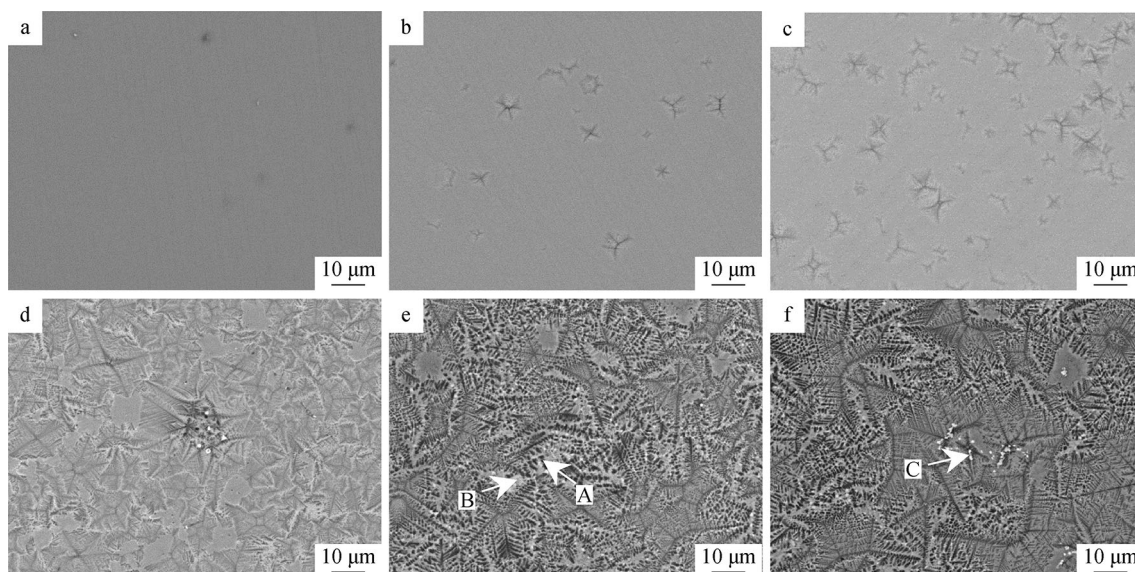


Fig. 2 SEM images of 2-mm rods for **a** Mn free, **b** 0.2 at% Mn, **c** 0.5 at% Mn, **d** 0.8 at% Mn, **e** 1.2 at% Mn and **f** 1.5 at% Mn-doped Mg–Zn–Ca alloys

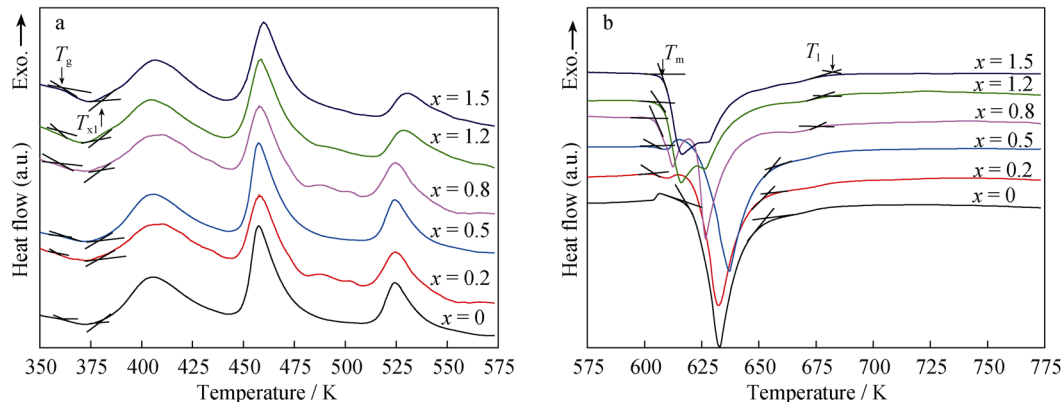
Table 1 EDS results of phases in Fig. 2e, f (at%)

Phases	Mg	Ca	Zn	Mn
A	77.91	2.57	19.01	0.51
B	56.94	3.75	39.31	–
C	45.82	1.50	11.85	40.83

Figure 3 demonstrates DSC curves of amorphous ribbons with a constant heating rate of 20 K·min⁻¹. It is clearly noted that all the ribbon samples go through a glass transition, followed by a supercooled liquid region. Then, similarly subsequent exothermic reactions due to crystallization can be observed. Based on DSC curve, the main thermal parameters, namely glass transition temperature (T_g), onset crystallization temperature (T_{x1}), melting temperature (T_m), and liquids temperature (T_l), as well as the values of ΔT_{x1} ($\Delta T_{x1} = T_x - T_g$) [25], T_{rg} ($T_{rg} = T_g/T_l$) [26], γ ($\gamma = T_{x1}/(T_g + T_l)$) [27], of these alloys are summarized in Table 2. Generally, the values of ΔT_{x1} , T_{rg} , and γ are used to evaluate the GFA of metallic glasses. Higher values of these indexes indicate a better GFA. In addition, critical size of the amorphous alloy prepared at the same condition is also widely recognized to characterize the GFA of alloys, and a larger critical size means a stronger

GFA. As can be seen from Figs. 1 and 2, the ribbon alloys of $(Mg_{65}Zn_{30}Ca_5)_{100-x}Mn_x$ ($x = 0, 0.2, 0.5, 0.8, 1.2, 1.5$; at%) are all in completely amorphous state, while the microstructure of 2-mm rod sample transfers from fully amorphous for the Mn-free alloy to almost polycrystalline state with precipitated phases. This indicates that the addition of Mn reduces the GFA of Mg–Zn–Ca alloy. However, it is found in Table 2 that the variation of supercooled liquid region (ΔT_{x1}) does not well agree with the change in GFA, while T_{rg} and γ decrease with the gradual addition of Mn, which is in well agreement with the changing trend of GFA in the present work.

In addition, Table 2 shows that the addition of Mn leads to the significant increment of liquid temperature (T_l) from 653.35 to 682.65 K and also the T_m and T_l intervals. Generally, a higher liquid temperature means that more energy can be distributed for nucleation and growth at the same solidification condition, which favors the precipitation of crystalline phases. This is in good agreement with the microstructure variation of the 2-mm rod samples in Fig. 2a–f. Furthermore, it is supposed that the composition of Mn-free alloy locates very close to the eutectic point, since it exhibits only one melting peak and the lowest T_l among the present alloys [28]. While for the Mn-added alloys, there are two or more melting peaks, suggesting the deviation of chemical composition from eutectic

**Fig. 3** DSC curves of $(Mg_{65}Zn_{30}Ca_5)_{100-x}Mn_x$ ribbons at heating rate of 20 K·min⁻¹: **a** 350–575 K and **b** 575–775 K**Table 2** Thermal parameters of amorphous ribbons of $(Mg_{65}Zn_{30}Ca_5)_{100-x}Mn_x$ alloys

Alloys	T_g /K	T_{x1} /K	T_m /K	T_l /K	ΔT_m /K	ΔT_x /K	T_{rg}	γ
$x = 0$	361.69	378.23	618.40	653.35	34.95	16.54	0.554	0.373
$x = 0.2$	360.65	378.88	604.88	654.59	49.71	18.23	0.551	0.373
$x = 0.5$	361.13	379.23	605.14	657.14	52.00	18.10	0.549	0.372
$x = 0.8$	360.23	382.51	604.91	676.08	71.17	22.28	0.532	0.369
$x = 1.2$	359.78	381.46	605.23	677.88	72.65	21.68	0.530	0.367
$x = 1.5$	361.52	382.05	606.81	682.65	75.84	20.53	0.529	0.366

composition. It is well known that the alloy whose composition locates at or is close to the eutectic point usually shows a higher GFA [26]. In this regard, the GFA of the Mg–Zn–Ca alloys is ruined with Mn addition.

It has been well known that the glass formation ability of the alloy is strongly dependent on the mixing enthalpy and atom size mismatch between the atoms in the alloy system, according to the empirical criteria for evaluating the glass-forming ability proposed by Inoue. A large negative mixing enthalpy would result in forming more stable or stronger atomic pair and/or clusters and increase the liquid viscosity [29]. Therefore, the difficulty of atom movement or diffusion would be increased, which can stabilize the supercooled liquid against crystallization. Large difference in atomic size ratio between components would enhance the packing density of atoms and clusters and retard the long-range rearrangement of atoms required for crystallization, thereby improving the GFA [30]. Thus, large negative mixing enthalpy and an atom size mismatch are favorable to the glass formation of the alloy.

Table 3 shows the mixing enthalpy and atomic radius of Mg, Zn, Ca and Mn elements. It can be seen that atomic size difference ratio of Mn between Mg, Zn and Ca are all larger than 19%, which satisfies the empirical criteria and would enhance the packing density of atoms and clusters. However, Mn has a large positive mixing enthalpy with Mg and Ca, which is unfavorable to the formation of strong atomic pair and/or clusters and stabilization of supercooled liquid. Therefore, crystalline phases tend to precipitate during solidification process. More amount of Mn addition would result in large content of crystalline phase. This is in accordance with XRD results in Fig. 1b and SEM analysis in Fig. 2. Based on the above discussion as well as the results of XRD and SEM of the rod samples, it can be concluded that the addition of Mn deteriorates the glass formation ability of Mg–Zn–Ca alloy.

3.2 Corrosion performance in SBF

The potentiodynamic polarization curves of $(\text{Mg}_{65}\text{Zn}_{30}\text{Ca}_5)_{100-x}\text{Mn}_x$ 2-mm rod samples as well as pure Mg (99.95 wt%) tested in SBF solution at 310 K are shown

in Fig. 4. Corrosion potential and corrosion current density obtained by Tafel extrapolation are summarized in Table 3. Generally, corrosion potential demonstrates the tendency to be corroded, while the value of corrosion current density indicates the level of corrosion rate. A more positive corrosion potential reflects a lower corrosion tendency, and a higher corrosion current density means the higher degradation or corrosion rate. As can be seen from Table 3, the Mn-free sample exhibits the noblest corrosion potential (-1.261 V) and the lowest corrosion current density ($49.325 \mu\text{A}\cdot\text{cm}^{-2}$). While for the 0.2 at% Mn-doped sample, there is a minor decrease in the corrosion potential and increase in the corrosion current density. Further addition of Mn leads to a further negative movement of the corrosion potential and increment of the corrosion current density of the Mn-doped samples. It is indicated that the corrosion resistance of the rod samples gradually decreases. In addition, as seen in Fig. 4 and Table 3, pure Mg exhibits the most negative corrosion potential (-1.657 V) and the largest corrosion current density ($459.453 \mu\text{A}\cdot\text{cm}^{-2}$). Although Mn addition decreases the corrosion resistance of Mg–Zn–Ca amorphous alloys, they still have higher corrosion resistance than pure Mg.

Figure 5 demonstrates the hydrogen evolution volume against immersion time for the 2-mm rod samples. It is noted that there is no obvious difference in hydrogen evolution volume for Mn-free and 0.2 at% Mn-doped samples within the whole immersion duration. It is suggested that the Mn-free sample and 0.2 at% Mn-doped sample exhibit a similar corrosion resistance, which is in agreement with the results of electrochemical test. However, with Mn addition increasing, hydrogen evolution volume of the rod samples (≥ 0.5 at% Mn) gradually increases, indicating that more Mn addition gradually weakens the corrosion resistance of $\text{Mg}_{65}\text{Zn}_{35}\text{Ca}_5$ alloy. Hydrogen evolution volume of pure Mg sample is also presented in Fig. 5. It can be seen that evolution volume of hydrogen of pure Mg is much higher than those of all the rod samples during the immersion duration. It is demonstrated that, although the addition of Mn deteriorates the corrosion resistance of Mg–Zn–Ca amorphous materials,

Table 3 Atomic size difference ratio and mixing enthalpy (ΔH^{mix}) of alloy elements

Elements	$\Delta H^{\text{mix}}/(\text{kJ}\cdot\text{mol}^{-1})$				Radius/nm	Atomic size difference ratio/%			
	Mg	Zn	Ca	Mn		Mg	Zn	Ca	Mn
Mg	–	– 4	– 6	12	0.160	–	13.13	18.78	30.00
Zn	– 4	–	– 22	– 6	0.139	13.13	–	29.44	19.42
Ca	– 6	– 22	–	19	0.197	18.78	29.44	–	43.15
Mn	– 4	– 21	1	–	0.112	30.00	19.42	43.15	–

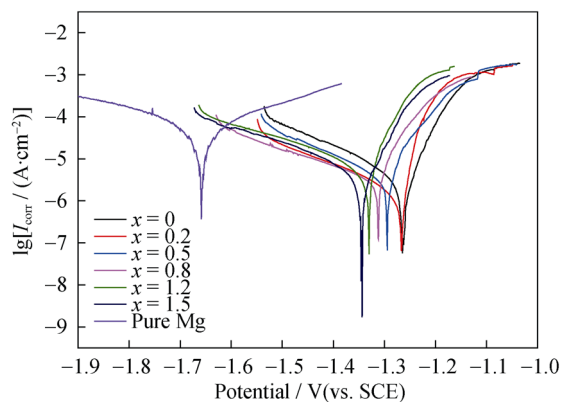


Fig. 4 Potentiodynamic polarization curves of $(\text{Mg}_{65}\text{Zn}_{30}\text{Ca}_5)_{100-x}\text{Mn}_x$ rods and pure Mg tested in SBF solution

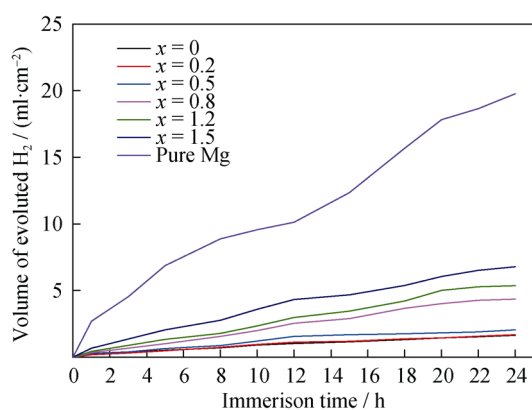


Fig. 5 Hydrogen evolution volume against immersion time of $(\text{Mg}_{65}\text{Zn}_{30}\text{Ca}_5)_{100-x}\text{Mn}_x$ rods and pure Mg immersed in SBF solution at 310 K

its composites still show a better corrosion performance than pure Mg.

Figure 6 shows surface morphologies of 2-mm rod samples for $(\text{Mg}_{65}\text{Zn}_{30}\text{Ca}_5)_{100-x}\text{Mn}_x$ alloys after 12-h immersion in SBF solution. A number of pits with different sizes are observed on the sample surface in Fig. 6a. Pits corrosion and non-uniform corrosion are the most common corrosion phenomena when Mg and its alloys are exposed into the solution with chloride ions [31]. The reason for pits corrosion can be attributed to the localized quenched-in defects, e.g., free volume, local variation in electrochemical activity, and inhomogeneities, formed during the rapid cooling process [28]. As seen in Fig. 6b for the addition of 0.2 at% Mn samples, the area subjected to corrosion significantly increases compared to Mn-free samples. In addition, some dendrite-like corrosion pits are clearly observed. In Fig. 6c for the 0.5 at% Mn-doped sample, it can be seen that the corrosion pits grow wider and deeper. As shown in Fig. 6d–f, with further Mn addition, corrosion off, crack, and collapse gradually occur, respectively. The variation of corrosion morphologies indicates that these

samples are corroded much more serious with Mn addition increasing, which is consistent with the results of electrochemical and hydrogen evolution tests in Figs. 4 and 5.

It was reported that trace impurity such as Fe, Ni, Cu, and Co in the conventional magnesium alloys acted as the cathodic sites and increased the cathodic efficiency [32, 33]. It is indicated that the existence of trace impurities increases the degradation rate, and thus the material is susceptible to localized corrosion attack in the initial period of immersion. MnCl_2 has been utilized to reduce the impurity content, especially Fe content (the main impurity in the conventional pure Mg) of industrially pure raw materials during alloy preparation [34]. In the present work, Mg–10 wt%Mn master alloy was employed with the hope of descending the impurities level and improving the corrosion resistance of the studied alloys. However, the results of electrochemical tests illustrate that Mn addition weakens the corrosion resistance, which is against the original intention. It is suggested that there may be some other factors playing more crucial roles on the corrosion performance of the studied alloys.

It is known that the performance of the materials is closely related to their microstructures. The decrease in the corrosion resistance in the present work can be attributed to the variation of microstructure with Mn addition. It is noted from Fig. 2 that $\text{Mg}_{65}\text{Zn}_{30}\text{Ca}_5$ sample exhibits a completely amorphous structure. The structure of amorphous materials is characterized as homogenization in chemical composition and absence of corrosion-induced microstructural defects like dislocations, secondary phases, and grain boundaries throughout the alloy. Galvanic corrosion can be greatly alleviated, and thus it exhibits the noblest corrosion potential and lowest corrosion current. It is demonstrated in Fig. 3 and Table 2 that the addition of Mn ruins the glass-forming ability of the Mg–Zn–Ca alloys. A minor addition (0.2 at%) of Mn leads to the fine dendrite phase precipitated in the amorphous matrix that the microstructure of the alloy turns from completely amorphous to partially amorphous. The newly precipitated dendrite phase is crystalline Mg phase (Fig. 2 and Table 1) which would form the micro-cell with the amorphous matrix, thus inducing the galvanic corrosion. Wang et al. [24] reported the corrosion behaviors of $\text{Mg}_{67}\text{Zn}_{28}\text{Ca}_5$ alloy with structures varying from amorphous to crystalline. They concluded that the partially amorphous structure with the produced $\text{Mg}_{102.8}\text{Zn}_{39.6}$ phase after the heat treatment improved the corrosion resistance. However, the generation of crystalline Mg leads to the less noble corrosion potential, an increase in corrosion current, and thus a decrease in corrosion resistance of alloy. This resulted from the more negative electrochemical potential of the crystalline Mg phase than that of the amorphous phase [35]. It can be seen from Figs. 1b and 2 that further

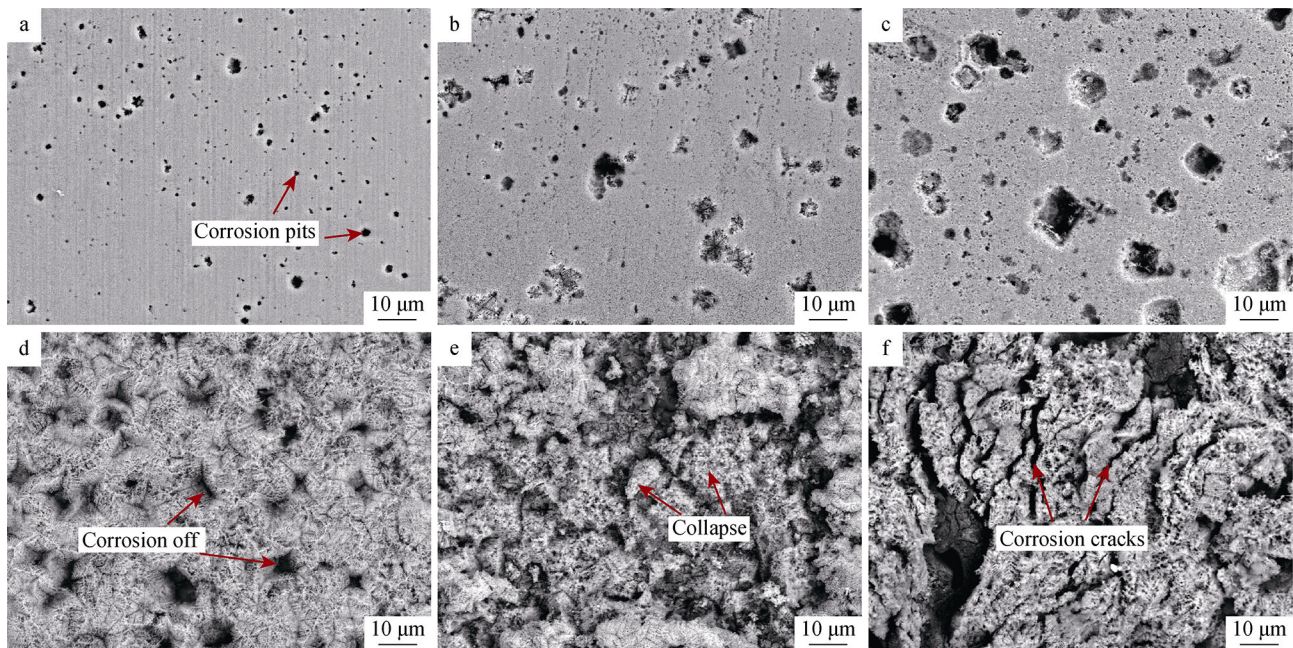


Fig. 6 Surface SEM images of 2-mm rod samples for **a** Mn free, **b** 0.2 at% Mn, **c** 0.5 at% Mn, **d** 0.8 at% Mn, **e** 1.2 at% Mn and **f** 1.5 at% Mn-doped Mg–Zn–Ca alloys after immersion in SBF for 12 h at 310 K

Table 4 Electrochemical parameter of $(\text{Mg}_{65}\text{Zn}_{30}\text{Ca}_5)_{100-x}\text{Mn}_x$ 2-mm rods with different structures

Samples	Structure	E_{corr}/V	$I_{\text{corr}}/(\mu\text{A}\cdot\text{cm}^{-2})$
$x = 0$	Completely amorphous	– 1.261	49.325
$x = 0.2$	Amorphous + Mg	– 1.264	52.853
$x = 0.5$	Amorphous + Mg	– 1.291	78.175
$x = 0.8$	Amorphous + Mg + Mn	– 1.313	98.417
$x = 1.2$	Mg + Mn + MgZn	– 1.330	142.255
$x = 1.5$	Mg + Mn + MgZn	– 1.344	159.089
Pure Mg	Mg	– 1.657	459.453

addition of Mn results in the gradual increase in the size and content of crystalline phases. These crystalline phases would form galvanic couples with amorphous matrix and become electrochemical corrosion sites when the samples are exposed to corrosion mediate. Consequently, the galvanic corrosion is gradually enhanced and the corrosion resistance is declined. That is to say, for Mg–Zn–Ca alloys in the present work, the Mn-doped samples prepared by injection show more negative corrosion potential and larger corrosion current density, as demonstrated in Table 4.

4 Conclusion

With Mn addition to $\text{Mg}_{65}\text{Zn}_{30}\text{Ca}_5$ alloy, all the ribbon samples are in amorphous state. While for the 2-mm rod

samples, their microstructure turns from fully amorphous to almost polycrystalline. The content and size of Mg, Mn, and MgZn precipitated phases increases with Mn addition increasing. Thus, the Mn addition ruins the glass-forming ability of $\text{Mg}_{65}\text{Zn}_{30}\text{Ca}_5$ alloy. The results of electrochemical, hydrogen evolution, and immersion tests for the 2-mm rod samples demonstrate that the precipitated crystalline phases induce the galvanic corrosion and decrease the corrosion resistance of $\text{Mg}_{65}\text{Zn}_{30}\text{Ca}_5$ alloy with Mn addition increasing. However, the rod samples prepared by copper mold injection method with partially amorphous structure still exhibit a much better corrosion resistance than the pure Mg.

Acknowledgements This study was financially supported by the National Natural Science Foundation of China (Nos. 51201120 and 51401155), the Science & Technology Coordination & Innovation Project of Shaanxi Province (No. 2016KTZDGY-04-01) and the Key Laboratory Program Funded by Shaanxi Provincial Education Department (No. 17JS053).

References

- [1] Hong D, Saha P, Chou DT, Lee B, Collins BE, Tan ZQ, Dong ZY, Kumta PN. In vitro degradation and cytotoxicity response of Mg–4%Zn–0.5%Zr (ZK40) alloy as a potential biodegradable material. *Acta Biomater.* 2013;9(10):8534.
- [2] Staiger MP, Pietak AM, Huadmai J, Dias G. Magnesium and its alloys as orthopedic biomaterials: a review. *Biomaterials.* 2006; 27(9):1728.
- [3] Vormann J. Magnesium: nutrition and metabolism. *Mol Aspects Med.* 2003;24(1–3):27.

- [4] Kraus T, Fischerauer SF, Hänzli AC, Uggowitz PJ, Löffler JF, Weinberg AM. Magnesium alloys for temporary implants in osteosynthesis: in vivo studies of their degradation and interaction with bone. *Acta Biomater.* 2012;8(3):1230.
- [5] Choi YI, Salman S, Kuroda K, Okido M. Improvement in corrosion characteristics of AZ31 Mg alloy by square pulse anodizing between transpassive and active regions. *Corros Sci.* 2012;63:5.
- [6] James M, Kumar S, Narayanan TSNS. Corrosion behavior of commercially pure Mg and ZM21 Mg alloy in Ringer's solution—long term evaluation by EIS. *Corros Sci.* 2011;53(2):645.
- [7] Erbel R, Di MC, Bartunek J, Bonnier J, Bruyne BD, Eberli FR, Erne P, Haude M, Heublein B, Horrigan M, Ilsley C, Böse D, Koolen J, Lüscher TF, Weissman N, Waksman R. Temporary scaffolding of coronary arteries with bioabsorbable magnesium stents: a prospective, non-randomised multicentre trial. *The Lancet.* 2007;369(9576):1869.
- [8] Witte F, Fischer J, Nellesen J, Crostack HA, Kaese V, Pisch A, Beckmann F, Windhagen H. In vitro and in vivo corrosion measurements of magnesium alloys. *Biomaterials.* 2006;27(7):1013.
- [9] Li H, Peng Q, Li X, Han ZS, Fang DQ. Microstructures, mechanical and cytocompatibility of degradable Mg–Zn based orthopedic biomaterials. *Mater Des.* 2014;58:43.
- [10] Yang Z, Yuan G, Zhang X, Mao L, Niu JL, Ding WJ. Comparison of biodegradable behaviors of AZ31 and Mg–Nd–Zn–Zr alloys in Hank's physiological solution. *Mater Sci Eng B.* 2012;177(5):395.
- [11] Zhang W, Li M, Chen Q, Hu WY, Zhang WM, Xin W. Effects of Sr and Sn on microstructure and corrosion resistance of Mg–Zr–Ca magnesium alloy for biomedical applications. *Mater Des.* 2012;39:379.
- [12] Gu Y, Bandopadhyay S, Chen CF, Ning CY, Guo YJ. Long-term corrosion inhibition mechanism of microarc oxidation coated AZ31 Mg alloys for biomedical applications. *Mater Des.* 2013;46:66.
- [13] Jiang WH, Jiang F, Green BA, Liu FX, Liaw PK. Electrochemical corrosion behavior of a Zr-based bulk-metallic glass. *Appl Phys Lett.* 2007;91(4):1177.
- [14] Gu X, Zheng Y, Zhong S, Xi TF, Wang JQ, Wang WH. Corrosion of, and cellular responses to Mg–Zn–Ca bulk metallic glasses. *Biomaterials.* 2010;31(6):1093.
- [15] Trumbo P, Yates AA, Schlicker S, Poos M. Dietary reference intakes: vitamin A, vitamin K, arsenic, boron, chromium, copper, iodine, iron, manganese, nickel, silicon, vanadium and zinc. *J Am Diet Assoc.* 2001;101(3):294.
- [16] Zberg B, Uggowitz PJ, Löffler JF. MgZnCa glasses without clinically observable hydrogen evolution for biodegradable implants. *Nat Mater.* 2009;8(11):887.
- [17] Ramya M, Sarwat SG, Udhayabanu V, Subramanian S, Raj B, Ravi KR. Role of partially amorphous structure and alloying elements on the corrosion behavior of Mg–Zn–Ca bulk metallic glass for biomedical applications. *Mater Des.* 2015;86:829.
- [18] Li HF, Pang SJ, Liu Y, Liaw PK, Zhang T. In vitro investigation of Mg–Zn–Ca–Ag bulk metallic glasses for biomedical applications. *J Non-Cryst Solids.* 2015;427:134.
- [19] Zhang E, Yin D, Xu L. Microstructure, mechanical and corrosion properties and biocompatibility of Mg–Zn–Mn alloys for biomedical application. *Mater Sci Eng C.* 2009;29(3):987.
- [20] Xu L, Yu GE, Pan F. In vivo corrosion behavior of Mg–Mn–Zn alloy for bone implant application. *J Biomed Mater Res A.* 2007;83(3):70.
- [21] Kakubo T, Takadama H. How useful is SBF in predicting in vivo bone bioactivity? *Biomaterials.* 2006;27(15):2907.
- [22] Song G. Control of biodegradation of biocompatible magnesium alloys. *Corros Sci.* 2007;49(4):1696.
- [23] Wang J, Li Y, Huang S. Effects of Y on the microstructure, mechanical and bio-corrosion properties of Mg–Zn–Ca bulk metallic glass. *J Mater Sci Technol.* 2014;30(12):1255.
- [24] Wang YS, Tan MJ, Pang JJ, Wang ZM, Jarfors AWE. In vitro corrosion behaviors of Mg₆₇Zn₂₈Ca₅ alloy: from amorphous to crystalline. *Mater Chem Phys.* 2012;134(2–3):1079.
- [25] Inoue A. Stabilization of metallic supercooled liquid and bulk amorphous alloys. *Acta Mater.* 2000;48(1):279.
- [26] Turnbull D. Under what conditions can a glass be formed? *Contemp Phys.* 1969;10(5):473.
- [27] Lu ZP, Liu CT. A new glass-forming ability criterion for bulk metallic glasses. *Acta Mater.* 2002;50(13):3501.
- [28] Zhang QS, Zhang HF, Deng YF, Ding BZ, Hu ZQ. Bulk metallic glass formation of Cu–Zr–Ti–Sn alloys. *Scr Mater.* 2003;49(4):273.
- [29] Xie KF, Yao KF, Huang TY. A Ti-based bulk glassy alloy with high strength and good glass forming ability. *Intermetallics.* 2010;18(10):1837.
- [30] Zhang ZY, Wu Y, Zhou J, Song WL, Cao D, Wang H, Liu XJ, Lu ZP. Effects of Sn addition on phase formation and mechanical properties of TiCu-based bulk metallic glass composites. *Intermetallics.* 2013;42(11):68.
- [31] Li Z, Gu X, Lou S, Zheng YF. The development of binary Mg–Ca alloys for use as biodegradable materials within bone. *Biomaterials.* 2008;29(10):1329.
- [32] Hofstetter J, Martinelli E, Pogatscher S, Schmutz P, Povoden-Karadeniz E, Weinberg AM, Uggowitz PJ, Löffler JF. Influence of trace impurities on the in vitro and in vivo degradation of biodegradable Mg–5Zn–0.3Ca alloys. *Acta Biomater.* 2015;23:347.
- [33] Li X, Liu X, Wu S, Yeung KWK, Zheng YF, Chu PK. Design of magnesium alloys with controllable degradation for biomedical implants: from bulk to surface. *Acta Biomater.* 2016;45:2.
- [34] Wu GH, Gao HT, Ding WJ, Zhu YP. Study on mechanism of iron reduction in magnesium alloy melt. *J Mater Sci.* 2005;40(23):6175.
- [35] Ahmad Z. Principles of Corrosion Engineering and Corrosion Control. Oxford: Butterworth-Heinemann; 2006. 20.